NANO LETTERS

2007
Vol. 7, No. 3
778−784

In-Situ Growth of Copper Sulfide Nanocrystals on Multiwalled Carbon Nanotubes and Their Application as Novel Solar Cell and Amperometric Glucose Sensor Materials

Hyunju Lee, Sang Won Yoon, Eun Joo Kim, and Jeunghee Park*

Department of Chemistry, Korea University, Jochiwon 339-700, Korea

Received December 27, 2006; Revised Manuscript Received February 11, 2007

ABSTRACT

Single-crystalline copper sulfide (β-Cu_2S) nanocrystals (NCs) were grown in situ on multiwalled carbon nanotubes (MWCNTs) by the solvothermal method. The morphology of the Cu_2S NCs was varied from spherical particles (av size = 4 nm) to triangular plates (av size = 12 nm) by increasing the concentration of the precursors. The lattice matching between Cu_2S and the MWCNTs would be an important factor in the growth of Cu_2S NCs on the MWCNTs. The solar cells and the amperometric glucose sensors fabricated using these Cu_2S–MWCNT hybrid nanostructures respond more sensitively than those using the Cu_2S NCs (or MWCNTs) alone. The utilization of the active Cu_2S NCs through direct binding with the conductive MWCNTs would lead to excellent performance of these nanodevices.

Since their discovery in 1991,[1] carbon nanotubes (CNTs) have attracted a tremendous amount of attention because of their extraordinary physical, chemical, and mechanical properties. Recently, significant interest has been directed toward the design of nanocrystal (NC) and CNT hybrid nanostructures in order to extend their range of applications to various energy conversion and sensing devices. In particular, semiconductor NC and CNT hybrid nanostructures, such as CdS−, CdSe−, and CdTe−CNTs, allow for the highly efficient generation of photocurrents via the interaction between excited NCs and conductive CNTs, thus demonstrating their importance as building blocks for light-harvesting assemblies.[2−5] It is also expected that they can be used to build biosensor platforms, owing to their greater ability to promote electron-transfer reactions with enzymes and other biomolecules. Pt, Pd, and Cu NCs deposited on CNTs have been shown to be excellent amperometric sensors for glucose over a wide range of concentrations.[6−9] Therefore, the exploration of novel NC−CNT hybrid nanostructures is a challenging subject because of their attractive combined properties of semiconductor (or metal) NCs and conductive CNTs.

In the copper sulfide system, there are several known solid phases: Cu_2S (chalcocite), $Cu_{1.96}S$ (djurleite), $Cu_{1.8}S$ (digenite), and CuS (covellite). All of these phases have been identified as p-type semiconducting materials because of the copper vacancies within the lattice.[10] Among them, Cu_2S has indirect and direct band gaps with E_g (bulk) = ∼1.2 and ∼1.8 eV,[10,11] respectively, and has been widely used as a component of solar cells, cold cathodes, and nanoscale switches.[12−14] Cu_2S and $Cu_{1.8}S$ NCs (nanoparticles, hexagonal nanoplates, nanorods, nanowires, etc.) have been synthesized by various methods.[15−21] However, the synthesis of Cu_2S−CNT hybrid nanostructures, via the direct growth of Cu_2S NCs on CNTs, has not yet been reported. Furthermore, a majority of the previous studies on NC−CNT nanostructures focused on establishing synthetic methods rather than on their controlled production allowing for the size and density of the NCs to be adjusted. Herein, we report a simple and straightforward in-situ synthetic route to prepare Cu_2S NC and multiwalled CNT (MWCNT) hybrid nanostructures with Cu_2S NCs having a controlled size/morphology/density on the surface of the MWCNTs. We also demonstrate their remarkable performance for applications involving both solar cells and electrochemical glucose sensors. The key to this application is the utilization of the active Cu_2S NCs in the electrical contact with the backing electrodes, through the conductive MWCNTs. We describe the construction of the devices, which respond even more sensitively than those fabricated using Cu_2S NCs and MWCNTs alone.

To prepare the Cu_2S−MWCNT hybrid nanostructures, acid-functionalized MWCNTs were used as ligands and templates to grow Cu_2S NCs by adapting the procedure

* Corresponding author. E-mail: parkjh@korea.ac.kr.

10.1021/nl0630539 CCC: $37.00
Published on Web 02/27/2007

developed by Zhang et al. to synthesize Cu_2S hexagonal nanoplates.[19] The MWCNTs were purchased from Iljin Nanotech Co., Ltd. (Korea). The surface modification of the CNT samples was achieved by refluxing them in a 3:1 mixture of HNO_3/H_2SO_4 for 2 h. They were then extensively washed with distilled water and dried using a vacuum oven. As a typical procedure to synthesize the Cu_2S-MWCNT hybrid nanostructures, 10 mg of the acid-functionalized MWCNTs was dispersed in 10 mL of dry oleylamine by ultrasonication, and then 0.25−2 mmol (0.066−0.53 g) of copper acetylacetonate ($Cu(acac)_2$) and 0.13−1 mmol (0.004−0.03 g) of elemental sulfur (S) were added in a ratio of 2:1 to a slightly heated solution of oleylamine. The resulting solution was heated to 190 °C, and the Cu_2S NCs were allowed to grow under vigorous stirring for 1−20 min. In the subsequent workup and purification, ethanol was added at 50 °C to precipitate Cu_2S-MWCNT. The wet precipitates were washed with chloroform and isolated by centrifugation to remove all of the free Cu_2S NCs. The precipitates were dried under vacuum at room temperature overnight, producing black Cu_2S-MWCNT. The free spherical Cu_2S NCs were synthesized under the same conditions, but without the MWCNTs. UV−vis spectroscopy (Scinco S-3100) and FTIR spectroscopy (ThermoNicolet Avatar 330) were used to identify the acid modification of the MWCNTs and in situ growth of the Cu_2S NCs. The products were characterized by scanning electron microscopy (SEM, Hitachi S-4300), field-emission transmission electron microscopy (FE TEM, FEI TECNAI G2 200 kV, and Jeol JEM 2100F), and high-voltage transmission electron microscopy (HVEM, Jeol JEM ARM 1300S, 1.25 MV). High-resolution X-ray diffraction (XRD) patterns were obtained using the 8C2 beam line of the Pohang Light Source (PLS) with monochromatic radiation (λ = 1.54520 Å). The XPS measurements were performed at the U7 beam line of the PLS.

Indium tin oxide (ITO)-coated glass substrates were cleaned by ultrasonication in acetone and soap solution, rinsed with deionized water, and then dried in an argon stream. Then they were deposited with a 50 nm-thick layer of poly(3,4-ethylenedioxylenethiophene)/polystyrene sulfonic acid (PEDOT/PSS). A solution of poly(3-octylthiophene) (P3OT) and Cu_2S-MWCNT nanostructures in chloroform was spun onto the PEDOT/PSS/ITO-coated glass substrate at 1500 rpm for 10 s, and the coated substrate was annealed under vacuum at 100 °C for 20 min. The average thickness of the active layer was 100 nm. Another set of photovoltaic devices was fabricated with an active layer, which consisted of Cu_2S NCs/P3OT (or MWCNTs/P3OT, Cu_2S NCs/MWCNTs blends/P3OT), prepared in the same manner. An aluminum (Al) back electrode (200 nm thick) was deposited through a shadow mask with an active area of approximately 0.09 cm^2. Power conversion efficiency measurements were carried out using a 1000-W solar simulator (Oriel) equipped with an AM1.5 optical filter employing an NREL-calibrated Si solar cell to adjust the light intensity to approximately 1 sun light intensity (1000 W/m^2). The IPCE was measured as a function of wavelength from 400 to 800 nm using an IPCE system (PV measurement, Inc.). Calibration was performed using a silicon reference photodiode (G587), and the IPCE values were collected at a low chopping speed of 5 Hz.

Glassy carbon (GC) electrodes (3-mm diameter, BAS) were carefully polished with a diamond pad/3 μm diamond polishing suspension, rinsed with distilled water and ethanol, and then dried under ambient nitrogen gas. Cu_2S-MWCNT (2−15 mg) was dissolved in a mixture of 0.1 mL Nafion perfluorosulfonated ion-exchange resin (Sigma-Aldrich, 5 wt %) and 0.9 mL of distilled water. About 60 min of ultrasonication was necessary to obtain uniformly dispersed Cu_2S-MWCNT. After dropping 10 μL of the Cu_2S-MWCNT solution onto the electrode surface, the electrode was dried in air. The GC electrode was modified by Nafion alone, Nafion mixed with the blend of Cu_2S NCs and MWCNTs (1:9 ratio), Cu_2S NCs, and acid-functionalized NWCNTs. The same weight was used for all of these nanostructures.

Cyclic voltammetry (CV) and chronoamperometry (CA) measurements were performed using an electrochemical analyzer (Epsilon, BAS). A Pt-wire auxiliary electrode and a Ag/AgCl standard reference electrode (Sigma-Aldrich) were used as the counter and reference electrodes, respectively. Using the modified-GC working electrode, the CV and CA data were measured in a mixture of 1 mM H_2O_2 and 20 mM phosphate buffer solution (PBS, pH 7.2). The constant-potential amperometry measurements required the prepositioning (~300 s) and operation of the electrode at a constant applied potential of 0.55 V versus Ag/AgCl. Once the current reached a baseline in the absence of H_2O_2 (or glucose), H_2O_2 (or glucose) was added every minute thereafter. The CV measurement was also carried out in a solution of 20 mM $K_4Fe(CN)_6$ and 0.2 M potassium chloride (KCl) as the supporting electrolyte.

For the glucose sensor, an enzyme solution was prepared by dissolving 1 mg of glucose oxidase (GOx, type VII from *Aspergillus niger*, 50000 UN) in a mixture of Cu_2S-MWCNT, Nafion, and distilled water. The glassy carbon electrode was then modified by adding an 8 μL drop of this enzyme solution and dried/stored at 4 °C. The CV and CA measurements were carried out in 50 mM PBS. Various concentrations of D(+)glucose (Sigma-Aldrich 97%, remainder primarily anomer), were prepared in 50 mM phosphate buffer at pH 7.2 and 4 °C.

The size and morphology of the Cu_2S NCs depend strongly on the concentration of the precursors ($Cu(acac)_2$ and S). When the concentration of the Cu_2S precursor, $Cu(acac)_2$, is below 0.1 M, the Cu_2S NCs are all spherical in shape. The TEM image of the Cu_2S-MWCNT nanostructures, synthesized using 0.05 M $Cu(acac)_2$, is displayed in Figure 1a. All of the MWCNTs are decorated homogeneously with Cu_2S NCs. The size range of the spherical Cu_2S NCs is 3−5 nm with an average value of 4 nm (Figure 1b). These spherical single-crystalline Cu_2S NCs are tightly bound to the graphite layers of the MWCNTs. The (002) planes of the Cu_2S NCs with d = 0.34 nm (JCPDS no. 26-1116; a = 3.961 Å, c = 6.722 Å) are parallel to the (002) planes of the graphite layers (d = 0.34 nm) in the MWCNTs (Figure 1c).

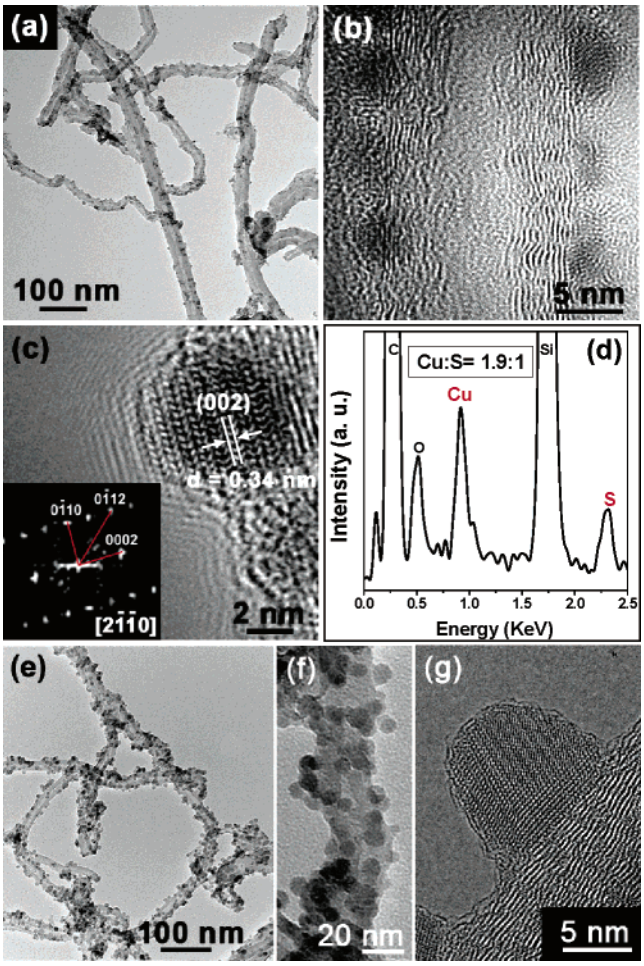

Figure 1. TEM and HRTEM images of Cu_2S−MWCNT, synthesized using 0.05 M $Cu(acac)_2$. (a) Cu_2S NCs are decorated homogeneously over all of the MWCNTs. (b) The size of the spherical Cu_2S NCs is uniformly 4 ± 1 nm. (c) The single-crystalline Cu_2S NC binds tightly to the wall of the MWCNT, with the (002) planes parallel to the wall. The corresponding FFT ED pattern is shown in the inset. (d) EDX confirms that Cu/S = ∼2:1. (e) Higher-density Cu_2S NCs, synthesized using 0.10 M $Cu(acac)_2$, cover the surface of the MWCNTs. (f) The size of the spherical Cu_2S NCs is 8 ± 1 nm. (g) The single-crystalline Cu_2S NC binds tightly to the wall of the MWCNT.

The corresponding fast Fourier transform ED (FFT ED) pattern reveals the hexagonal unit cell of the β-Cu_2S NCs, whose [0002] direction is perpendicular to the wall of the MWCNTs (inset). The EDX analysis confirms that the NCs consisted of Cu and S in a ratio of (1.9 ± 0.1):1 (Figure 1d). The C and O peaks originate from the MWCNTs, and the Si peak comes from the Si TEM grid. Figure 1e shows the Cu_2S−MWCNT hybrid nanostructures, synthesized using 0.10 M $Cu(acac)_2$. The MWCNTs are fully covered with the higher-density Cu_2S NCs. The magnified image reveals that they have an average size of 8 ± 1 nm (Figure 1f). The atomic-resolution image reveals the highly crystalline 9-nm Cu_2S NCs attached to the graphite layers in the MWCNTs (Figure 1g). We observed that the size and density of the NCs increase simultaneously with increasing concentration of the precursor.

As the concentration of $Cu(acac)_2$ is increased to 0.15 M, the average size of the NCs increases continuously to 12 nm, the triangular morphology becomes dominant, and the density decreases as compared to that produced at a lower concentration of precursors. Figure 2a shows the Cu_2S−MWCNT hybrid nanostructures, synthesized using 0.15 M $Cu(acac)_2$. It can be seen that the triangularly shaped Cu_2S NCs grew on the MWCNTs. One face of these triangular Cu_2S NCs is usually bound to the wall of the MWCNTs. All of the triangular NCs have three equilateral edges with a length of 10−14 nm. The HRTEM image of a triangular Cu_2S NC confirms that it consists of an equilaterally edged single-crystalline Cu_2S crystal (Figure 2b). The corresponding FFT ED pattern reveals that the $[\bar{1}\bar{1}20]$ direction of the hexagonal unit cell at the $[\bar{1}100]$ zone axis is tilted toward the wall of the MWCNTs by an angle of ∼30° (inset). To examine the crystal structure of these triangular NCs thoroughly, a detached triangular NC from the MWCNTs (in a washed solution) was selected, as shown in Figure 2c. It has unquestionably flat side planes with a thickness of 2 nm, revealing its "plate" morphology. The corresponding FFT ED pattern, shown in the inset of Figure 2c, is identical to that of Figure 2b. These NCs have three triangular edges along the $[\bar{1}\bar{1}20]$, $[\bar{1}2\bar{1}0]$, and $[2\bar{1}\bar{1}0]$ directions. The interplanar spacing between the adjacent (110) planes is identified as being 0.20 nm, which is consistent with that of bulk β-Cu_2S crystals. The TEM image taken in the [0001] zone axis reveals that the (120) planes of the Cu_2S triangular nanoplates are probably parallel to the walls of the MWCNTs.

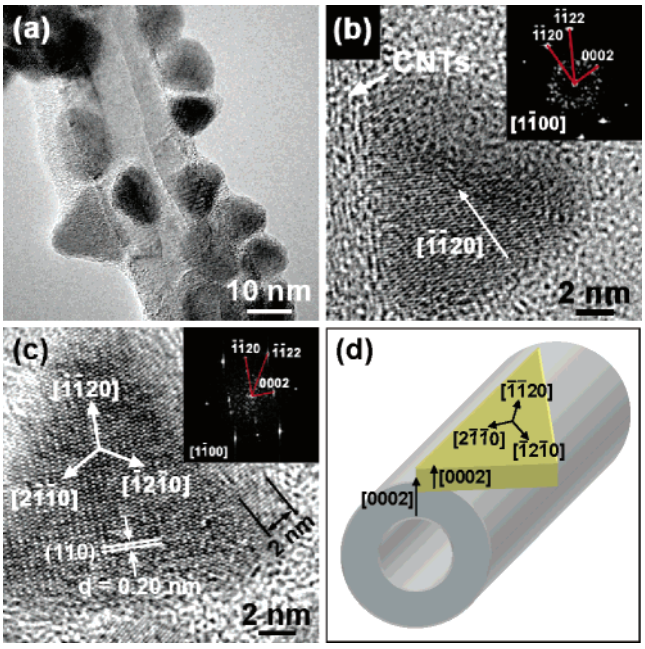

Figure 2. TEM and HRTEM images of the Cu_2S−MWCNT synthesized using 0.15 M $Cu(acac)_2$. (a) Triangularly shaped Cu_2S NCs are grown on the MWCNTs. All of the NCs have highly symmetric triangular morphology with three equilateral edges having a length of 12 ± 2 nm. (b) One face of the triangular NC is bound to the wall of the MWCNTs. The inset corresponds to the FFT ED pattern. (c) A detached triangular NC from the MWCNTs shows flat side edges with a thickness of 2 nm. Its corresponding FFT ED pattern is shown in the inset. (d) A schematic diagram showing the crystal structure of the triangular nanoplates attached to the MWCNTs.

The nanoplates tend to be self-assembled when the higher concentration of precursor (0.2 M $Cu(acac)_2$) is used (Supporting Information, Figure S1). The (001) planes parallel to the side planes were identified by the HRTEM and ED patterns.

Huang and Gao reported the growth of CdS and TiO_2 NCs on MWCNTs and explained their findings by the lattice matching of the cubic CdS (111) and rutile TiO_2 (110) planes with the (002) graphite planes of the CNTs.[22,23] In the present case, the interlayer distance of the (002) planes of β-Cu_2S (3.361 Å) exactly matches that of the (002) graphite planes of the CNTs (3.395 Å). Therefore, the CNTs may act as templates and/or substrates for the growth of Cu_2S NCs along the [0002] direction, as shown in Figure 1c. The surface defect sites of the MWCNTs would allow for the deposition of the Cu_2S NCs. With regard to the Cu_2S triangular nanoplates attached to the MWCNTs, we suggest that the (002) planes of the Cu_2S side planes could be jointed with those of the graphite layers in the CNTs, as shown in the schematic diagram of Figure 2d. Moreover, there is a small lattice mismatch (4.7%) between the (120) plane of β-Cu_2S (1.2965 Å) and the (110) plane of CNTs (1.2350 Å), which may determine the direction of triangular facets.

A triangular nanoplate morphology was reported for CdS,[24,25] NiS,[26] LaF_3,[27] CoO,[28] ZnO,[29] Au,[30,31] Ag,[32,33] and Pd[34] but not for Cu_2S. The crystal structure of the Cu_2S triangular nanoplates (enclosed with the $[\bar{1}\bar{1}20]$, $[\bar{1}2\bar{1}0]$, and $[2\bar{1}\bar{1}0]$ directions) is the same as that of trigonal LaF_3 and hexagonal ZnO.[27,29] Interestingly, we were not able to obtain any triangular nanoplates under the same conditions in the absence of the MWCNTs. The formation of triangular nanoplates at a higher concentration may be explained by the kinetically controlled growth mechanism, which is assisted by lattice matching with the graphite layers of the MWCNTs. Even so, the growth feature of the Cu_2S nanoplates on the surface of the MWCNTs needs further investigation.

Additional evidence for the formation of Cu_2S NCs on the surface of the MWCNTs comes from the XRD measurements (Figure 3a). The XRD patterns of the MWCNTs (acid-functionalized) and free Cu_2S NCs samples were also measured. The free spherically shaped Cu_2S NCs (size = 7−9 nm with an average value of 8 nm) were synthesized under the same conditions without the MWCNTs, and their TEM image is shown in the inset. The MWCNTs show the typical (002) and (100) peaks of graphite, whereas the free Cu_2S NCs show peaks corresponding to hexagonal chalcocite β-Cu_2S (JCPDS no. 26-1116; a = 3.961 Å, c = 6.722 Å). The Cu_2S NC (av size = 8 nm)−MWCNT hybrid nanostructures sample, whose TEM images are shown in Figure 1e, shows the same peaks as those observed for the free Cu_2S NCs. The (002) peaks of β-Cu_2S and graphite overlapped each other. Using the Debye−Scherrer equation, the average size of the Cu_2S triangular nanoplates was estimated to be 10 nm for Cu_2S−MWCNT, which is consistent with the TEM images. The weak peaks between 30 and 40° (marked by the symbol *) are thought to be caused by the surplus sulfur on the surface of the Cu_2S NCs.

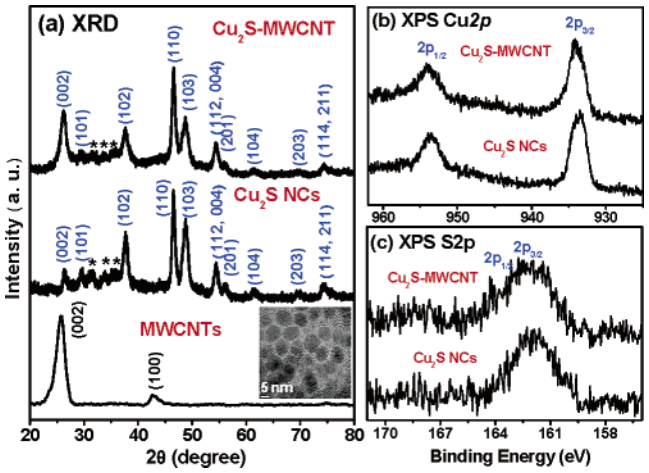

Figure 3. (a) XRD patterns for acid-functionalized MWCNTs, free Cu_2S NCs, and Cu_2S−MWCNT. The inset displays the TEM image of free Cu_2S NCs. Fine-scanned XPS of (b) Cu $2p_{1/2}$ and $2p_{3/2}$ and (c) S $2p_{1/2}$ and $2p_{3/2}$ of free Cu_2S NCs and Cu_2S−MWCNT.

The XPS measurements also established the formation of Cu_2S NCs on the MWCNT surface. The full-range XPS spectrum of Cu_2S−MWCNT shows the presence of C, Cu, O, and S components (Supporting Information, Figure S2a). The fine-scanned Cu $2p_{3/2}$ and $2p_{1/2}$ peaks are displayed in Figure 3b, along with those of free Cu_2S NCs. These two peaks become slightly broader when the NCs are grown on the MWCNTs. The unresolved S $2p_{3/2}$−$2p_{1/2}$ peak of Cu_2S−MWCNT also shows a broader width than that of free Cu_2S NCs (Figure 3c). This broadening may be due to the interaction of their electronic states with those of the graphite layers. There is no obvious shoulder in the higher-energy region because of surface oxidation, implying that the surfaces of the Cu_2S NCs are stable. The full range and fine-scanned O 1s peaks of free Cu_2S NCs and Cu_2S−MWCNT are displayed in the Supporting Information (Figure S2b). We also measured the Raman spectra in order to confirm the presence of pure Cu_2S crystals, as shown in the Supporting Information (Figure S3).

We fabricated polymer solar cells by using blends of various weight percentages of Cu_2S−MWCNT and P3OT as the active layers. Incident photon-to-current conversion efficiencies (IPCE) were measured for the P3OT and Cu_2S−MWCNT/P3OT devices (Figure 4a). The active layers contain 10 wt % Cu_2S−MWCNT in the polymer blends, where the Cu_2S NCs have an average size of 8 nm along with a maximum density (as shown in Figure 1e). We were not able to measure an IPCE curve for the 10 wt % MWCNT/P3OT devices, probably because of the inhomogeneous blending of the composites. The presence of Cu_2S−MWCNT nanostructures results in an enhancement of the IPCE over the whole wavelength range of 400−800 nm. The UV−visible spectrum of the composites was also measured to show the enhancement of absorbance due to the Cu_2S NCs (Supporting Information, Figure S4).

We performed current−voltage (I−V) measurements for these ITO/PEDOT/PSS/Cu_2S−MWCNT (10 wt %)/P3OT/Al solar cell devices. Figure 4b corresponds to the I−V characterization curve of the solar cell device exhibiting the

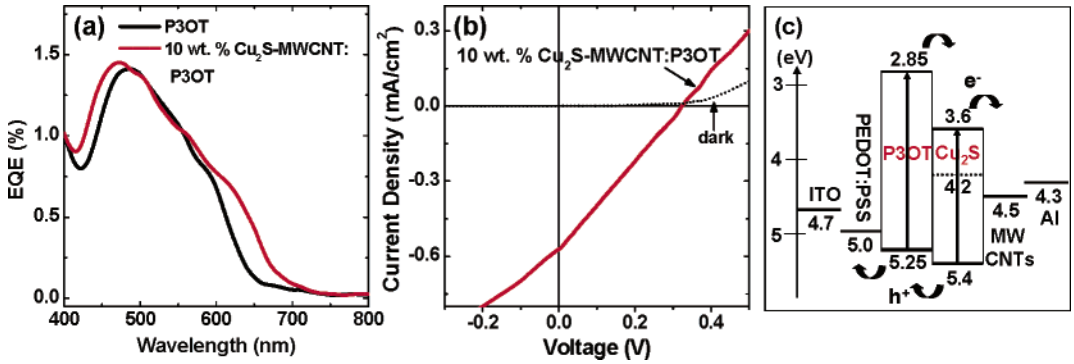

Figure 4. (a) IPCE of the solar cell devices using P3OT and Cu_2S−MWCNT/P3OT as active layers. (b) Current density (mA/cm^2) vs applied voltage (V) for the ITO/PEDOT/PSS/Cu_2S−MWCNT/P3OT/Al solar cell operated under AM 1.5 illumination, with a solar power conversion efficiency of 0.08%. (c) Energy diagram of the valence- and conduction-band levels showing the charge-transfer junction formed in this solar cell device.

maximum power conversion efficiency. The short-circuit current density (J_{SC}), open-circuit voltage (V_{OC}), fill factor (FF), and power conversion efficiency ($\eta = J_{SC} \times V_{OC} \times FF/I_{light}$) of the solar cell devices are 0.57 mA/cm^2, 0.32 V, 44%, and 0.08%, respectively, under AM 1.5 conditions. The $I-V$ characterization of the photovoltaic devices fabricated using Cu_2S NCs/P3OT (or MWCNTs/P3OT, Cu_2S NCs/MWCNTs/P3OT) was also performed, but their power conversion efficiency was found to be below the detection limit (<0.01%). The power conversion efficiency (0.08%) is higher than that (0.04%) of SWCNTs/P3OT photovoltaic devices,[35] so these hybrid nanostructures are potentially useful in optoelectronic applications.

We can offer no firm explanation for the enhanced photocurrent of the Cu_2S−MWCNT hybrid nanostructures as compared to that of Cu_2S NCs (or MWCNTs) alone or Cu_2S NCs/MWCNTs blends; however, the possible origin of these observations can be inferred on the basis of the known properties of CNTs. P3OT produces photogenerated electron−hole pairs. The Cu_2S NCs would be expected to accept the electrons from the P3OT and also generate electron−hole pairs mainly via the direct band gap, following the absorption of photon energy in the UV−visible range. The MWCNTs attached directly to the Cu_2S NCs may facilitate the generation of a photocurrent by trapping the conduction-band electrons, a process that results in charge separation and retardation of the recombination process. That is, the highly conductive CNTs provide direct and efficient paths for the transport of conduction-band electrons to the Al electrode. However, PEDOT/PSS may act as a hole acceptor, thus helping to regenerate the P3OT and Cu_2S ground states by delivering the holes to the ITO electrode. The energy diagram of the valence- and conduction-band levels shown in Figure 4c illustrates the charge-transfer junction between the Cu_2S, MWCNT, P3OT, PEDOT/PSS, and ITO/Al electrodes. We assume that the band gap and Fermi level of Cu_2S are the same as those of bulk Cu_2S.[10,11] For the solar cell system consisting of CdSe−SWCNT or only SWCNTs blended with P3OT, it was suggested that the semiconducting SWCNTs help to transport the photoexcited electrons efficiently from the NCs or P3OT to the positive electrode.[4,35] The present work indicates that the MWCNTs can also serve as efficient electron acceptors from the excited Cu_2S NCs, and this hypothesis is supported by recent work involving the ZnS NCs−MWCNT systems.[36]

For the development of an amperometric biosensor for glucose, the Cu_2S−MWCNT hybrid nanostructures were solubilized in Nafion, a perfluorosulfonated polymer, to facilitate the modification of the GC electrode surface.[37,38] Nafion also acts as an immobilizing matrix for GOx, which is used for efficiently monitoring the direct electroactivity of GOx at the electrode surface. The amperometric detection of H_2O_2 is preliminarily performed because H_2O_2 is released during the oxidation of glucose by GOx in the presence of oxygen. Figure 5a represents the steady-state cyclic voltammetry (CV) for the four modified GC electrodes, viz., Nafion mixed with the Cu_2S−MWCNT hybrid nanostructures, Cu_2S NCs, MWCNTs (acid-functionalized), and the Cu_2S NCs/MWCNT blend, in 1 mM H_2O_2/PBS at a scan rate of 50 mV s^{-1}. The same weight was used to compare the electrochemical activity toward the redox of H_2O_2. The Cu_2S−MWCNT-based electrode (curve A) exhibits the well-defined oxidation and reduction peaks of H_2O_2 at +0.39 and +0.15 V in the forward and reverse scans, respectively. The Cu_2S NC-based electrode (curve B) shows no current, as is also the case for the Nafion-only modified electrode (not displayed here). The MWCNT-based electrode (curve C) displays almost no redox waves, but the resultant current is higher than that of curve B, indicating the existence of an electrical contact between the MWCNTs and the GC backing electrode. The GC electrode modified with the Cu_2S NCs/MWCNTs blend, which mimics the Cu_2S−MWCNT hybrid nanostructure, exhibits a higher current level with a noticeable redox wave. Nevertheless, the resultant current is lower than that of curve A by a factor of 1/10.

Figure 5b displays the amperometric response of the Cu_2S−MWCNT/Nafion-modified GC electrodes upon the addition of H_2O_2 solution. The inset shows that the response is linear for an H_2O_2 concentration between 50 nM and 10 μM. The linear response of the electrodes to H_2O_2 corresponds to a sensitivity of 125 nA/mM. The response time and detection limit ($S/N = \sim 3$) are determined to be 3 s and 50 nM, respectively. The repeated use of the electrodes did not affect their long-term stability as long as the measurement

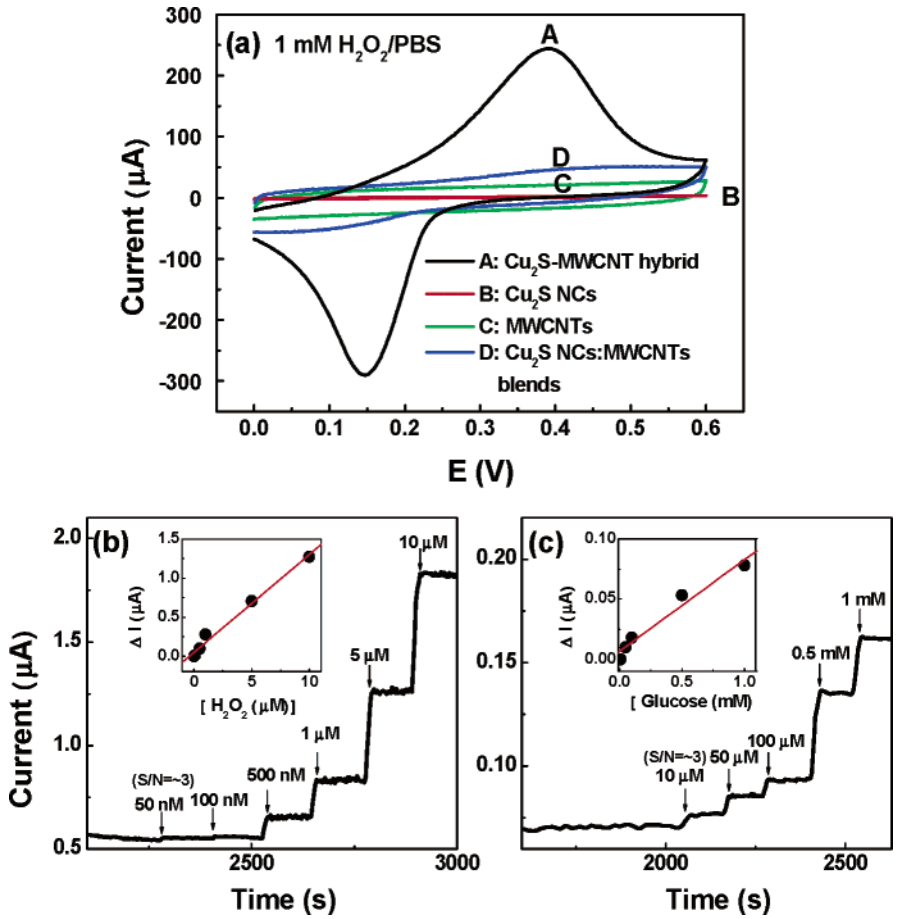

Figure 5. (a) CV performance of (A) Cu_2S−MWCNT/Nafion-, (B) Cu_2S NCs/Nafion-, (C) MWCNTs/Nafion-, and (D) Cu_2S NCs/MWCNTs/Nafion-modified GC electrodes in the amperometric detection of 1 mM H_2O_2 in 50 mM phosphate buffer (pH 7.2) vs the Ag/AgCl (3 M NaCl) reference electrode (at a scan rate of 20 mV s^{-1}). (b) CA response of Cu_2S−MWCNT/Nafion-modified GC electrodes at 0.55 V upon subsequent addition of H_2O_2 solution. The inset shows a linear response for H_2O_2 concentrations between 50 nM and 10 μM. (c) CA response of Cu_2S−MWCNT/GOx/Nafion electrodes upon the addition of glucose solution. The detection limit is 10 μM. The inset shows the linear response for glucose concentrations between 10 μM and 1 mM.

was not performed at a high concentration of H_2O_2 (>20 mM). The reproducibility of the current signal for five repeated injections of H_2O_2 was within 5%. The Cu_2S−MWCNT/GOx/Nafion-modified electrode was sensitive to the subsequent addition of glucose solution (Figure 5c). The inset shows a linear response for glucose concentrations between 10 μM and 1 mM. The detection limit ($^S/_N = \sim 3$) is determined to be 10 μM. This optimized glucose biosensor displays a sensitivity of 75 nA/mM. The detection limit of the Cu_2S−MWCNT-based GC electrode is comparable to that of the Pt NC−SWCNT/Nafion GC electrode reported by the Luong group.[6]

The large current of the Cu_2S−MWCNT hybrid nanostructures implies that they can be percolated well with Nafion so as to form an electrically conductive layer. They project outward from the electrode surfaces and act like nanoelectrodes that allow access to the embedded active sites and facilitate direct electron transfer. The higher current of the Cu_2S NCs/MWCNT blends as compared with that of the MWCNTs suggests that the Cu_2S NCs would have electrocatalytic activity toward the redox reaction of H_2O_2, as is the case with other metal NCs on MWCNTs.[6−9] Unfortunately, there have been no other reports of any catalytic activity of Cu_2S for the redox reaction of H_2O_2. However, complexes of Cu(I) ions with various ligands (especially sulfur ligands) have been recognized as systems presenting high activity toward the decomposition of H_2O_2.[39,40] Therefore, there is a possibility that the catalytic reaction of Cu(I) states (of Cu_2S NCs) involves a series of H_2O_2 redox reactions. Nevertheless, we suggest that the synergetic combination of the catalytic activity of the Cu_2S NCs and the electrical network formed through their direct binding with the MWCNTs would produce excellent electrochemical communication.

In addition, these modified electrodes exhibit efficient amperometric detection behavior for the Fe^{3+}/Fe^{2+} redox reaction. The CV was measured for 20 mM $Fe(CN)_6^{4-}$ and 0.2 M KCl at 50 mVs^{-1}, with well-defined oxidation and reduction peaks (Supporting Information, Figure S5). The Cu_2S−MWCNT hybrid nanostructures synthesized with the Cu_2S NCs having a controlled size/density exhibit the highest current when the density of the Cu_2S NCs is the largest (size = 8 nm). This result reconfirms that the Cu_2S NCs contribute to increasing the detection sensitivity of the redox reactions. We demonstrate that this unique Cu_2S−MWCNT hybrid

nanostructure constitutes a new class of electrode materials for various biosensing applications.

In summary, single-crystalline hexagonal-phase β-Cu_2S NCs were grown in situ on acid-functionalized MWCNTs by the solvothermal method. The morphology of the Cu_2S NCs was varied from spherical particles (av size = 4 nm) to triangular plates (av size = 12 nm) by increasing the concentration of the precursors. These triangular NCs have three edges along the $[\bar{1}\bar{1}20]$, $[\bar{1}2\bar{1}0]$, and $[2\bar{1}\bar{1}0]$ directions. The lattice matching between the (002) planes of Cu_2S and the (002) planes of the MWCNTs is thought to be an important factor in the growth of the Cu_2S NCs on the surface of the MWCNTs.

The photovoltaic device fabricated from the blends of Cu_2S−MWCNT and P3OT responds more sensitively than those fabricated using Cu_2S NCs (or MWCNTs) alone. The maximum power conversion efficiency was found to be η = 0.08%. Direct, efficient electron transport from the photoexcited Cu_2S NCs to the MWCNTs would enhance their photocurrents. The GC electrode modified with Cu_2S−MWCNT/Nafion responds more sensitively than those modified with Cu_2S NCs (or MWCNTs) and exhibits a linear response to H_2O_2 with a linear range of up to 10 μM and a detection limit of 50 nM. The optimized glucose sensor (with immobilized GOx) displays a linear range up to 1 mM and a detection limit of 10 μM. The synergetic combination of the catalytic activity of the Cu_2S NCs and the electrical network formed through direct bindings with the MWCNTs is responsible for this excellent electrochemical communication.

Acknowledgment. J.P. thanks Prof. Donghwan Kim (Division of Materials Science and Engineering, Korea University), Dr. Nam-Gyu Park (Materials Science & Technology Division, Korea Institute of Science and Technology), and Dr. Jae Pyung Ahn (Nano-Material Research Center, Korea Institute of Science and Technology) for helpful technical support. This work was supported by KRF grants (R14-2003-033-01003-0, R02-2004-000-10025-0, and 2003-015 C00265) and BK21. The SEM, HVEM, XRD, and XPS measurements were performed at the Korea Basic Science Institute. The experiments at the PLS were partially supported by MOST and POSTECH.

Supporting Information Available: TEM images of self-assembled triangular NCs; full-range and O 1s XPS spectra of free Cu_2S NCs and Cu_2S−MWCNT hybrid nanostructures; Raman spectra of MWCNTs and Cu_2S−MWCNT hybrid nanostructures; UV−visible absorption spectra of pure P3OT, MWCNTs/P3OT, Cu_2S NCs/P3OT, and Cu_2S−MWCNT/P3OT composites; and CV data of modified GC electrodes for the Fe^{3+}/Fe^{2+} redox reaction. This material is available free of charge via the Internet at http://pubs.acs.org.

References

(1) Iijima, S. *Nature* **1991**, *354*, 56.
(2) Sheeney-Haj-Ichia, L.; Basnar, B.; Willner, I. *Angew. Chem., Int. Ed.* **2005**, *44*, 78.
(3) Robel, I.; Bunker, B. A.; Kamat, P. V. *Adv. Mater*. **2005**, *17*, 2458.
(4) Landi, B. J.; Castro, S. L.; Ruf, H. J.; Evans, C. M.; Bailey, S. G.; Raffaelle, R. P. *Sol. Energy Mater. Sol. Cells* **2005**, *87*, 733.
(5) Guldi, D. M.; Aminur Rahman, G. M.; Sgobba, V.; Kotov, N. A.; Bonifazi, D.; Prato, M. *J. Am. Chem. Soc*. **2006**, *128*, 2315.
(6) Hrapovic, S.; Liu, Y.; Male, K. B.; Luong, J. H. T. *Anal. Chem*. **2004**, *76*, 1083.
(7) Yang, M.; Yang, Y.; Liu, Y.; Shen, G.; Yu, R. *Biosens. Bioelectron.* **2006**, *21*, 1125.
(8) Lim, S. H.; Wei, J.; Lin, J.; Li, Q.; You, J. K. *Biosens. Bioelectron.* **2005**, *20*, 2341.
(9) Male, K. B.; Hrapovic, S.; Liu, Y.; Wang, D.; Luong, J. H. T. *Anal. Chim. Acta* **2004**, *516*, 35.
(10) Liu, G.; Schulmeyer, T.; Brötz, J.; Klein, A.; Jaegermann, W. *Thin Solid Films* **2003**, *431*−*432*, 477.
(11) He, Y.; Kriegseis, W.; Bläsing, J.; Polity, A.; Krämer, T.; Hasselkamp, D.; Meyer, B. K.; Hardt, M.; Krost, A. *Jpn. J. Appl. Phys.* **2002**, *41*, 4630.
(12) Neville, R. C. *Solar Energy Conversion: The Solar Cell*, 2nd ed.; Elsevier: Amsterdam, 1995.
(13) Xu, N. S.; Huq, S. E. *Mater. Sci. Eng., R* **2005**, *48*, 47.
(14) Sakamoto, T.; Sunamura, H.; Kawaura, H.; Hasegawa, T.; Nakayama, T.; Aono, M. *Appl. Phys. Lett*. **2003**, *82*, 3032.
(15) (a) Sigman, M. B., Jr.; Ghezelbash, A.; Hanrath, T.; Saunders, A. E.; Lee, F.; Korgel, B. A. *J. Am. Chem. Soc.* **2003**, *125*, 16050. (b) Larsen, T. H.; Sigman, M.; Ghezelbash, A.; Doty, R. C.; Korgel, B. A. *J. Am. Chem. Soc*. **2003**, *125*, 5638. (c) Ghezelbash, A.; Korgel, B. A. *Langmuir* **2005**, *21*, 9451.
(16) Lou, Y.; Samia, A. C. S.; Cowen, J.; Banger, K.; Chen, X.; Lee, H.; Burda, C. *Phys. Chem. Chem. Phys.* **2003**, *5*, 1091.
(17) Chen, L.; Chen, Y.-B.; Wu, L.-M. *J. Am. Chem. Soc.* **2004**, *126*, 16334.
(18) (a) Liu, Z.; Liang, J.; Xu, D.; Lu, J.; Qian, Y. *Chem. Commun.* **2004**, 2724. (b) Liu, Z.; Xu, D.; Liang, J.; Shen, J.; Zhang, S.; Qian, Y. *J. Phys. Chem. B* **2005**, *109*, 10699.
(19) Zhang, H.-T.; Wu, G.; Chen, X.-H. *Langmuir* **2005**, *21*, 4281.
(20) Li, Z.; Yang, H.; Ding, Y.; Xiong, Y.; Xie, Y. *Dalton Trans*. **2006**, 149.
(21) Zhang, H.-X.; Ge, J.-P.; Li, Y.-D. *J. Phys. Chem. B* **2006**, *110*, 14107.
(22) Huang, Q.; Gao, L. *Nanotechnology* **2004**, *15*, 1855.
(23) Huang, Q.; Gao, L. *J. Mater. Chem.* **2003**, *13*, 1517.
(24) Pinna, N.; Weiss, K.; Urban, J.; Pileni, M.-P. *Adv. Mater*. **2001**, *13*, 261.
(25) Warner, J. H.; Tilley, R. D. *Adv. Mater.* **2005**, *17*, 2997.
(26) Ghezelbash, A.; Sigman, M. B., Jr.; Korgel, B. A. *Nano Lett*. **2004**, *4*, 537.
(27) Zhang, Y.-W.; Sun, X.; Si, R.; You, L.-P.; Yan, C.-H. *J. Am. Chem. Soc*. **2005**, *127*, 3260.
(28) Seo, W. S.; Shim, J. H.; Oh, S. J.; Lee, E. K.; Hur, N. H.; Park, J. T. *J. Am. Chem. Soc*. **2005**, *127*, 6188.
(29) Andelman, T.; Gong, Y.; Polking, M.; Yin, M.; Kuskovsky, I.; Neumark, G.; O'Brien, S. *J. Phys. Chem. B* **2005**, *109*, 14314.
(30) Li, C.; Cai, W.; Cao, B.; Sun, F.; Li, Y.; Kan, C.; Zhang, L. *Adv. Funct. Mater*. **2006**, *16*, 83.
(31) Chu, H.-C.; Kuo, C.-H.; Huang, M. H. *Inorg. Chem*. **2006**, *45*, 808.
(32) (a) Sun, Y.; Xia, Y. *Adv. Mater.* **2003**, *15*, 695. (b) Washio, I.; Xiong, Y.; Yin, Y.; Xia, Y. *Adv. Mater.* **2006**, *18*, 1745.
(33) Chen, S.; Carroll, D. L. *Nano Lett.* **2002**, *2*, 1003.
(34) Xiong, Y.; McLellan, J. M.; Chen, J.; Yin, Y.; Li, Z.-Y.; Xia, Y. *J. Am. Chem. Soc.* **2005**, *127*, 17118.
(35) Kymakis, E.; Amaratunga, G. A. J. *Appl. Phys. Lett.* **2002**, *80*, 112.
(36) Du, J.; Fu, L.; Liu, Z.; Han, B.; Li, Z.; Liu, Y.; Sun, Z.; Zhu, D. *J. Phys. Chem. B* **2005**, *109*, 12772.
(37) Wang, J.; Musameh, M.; Lin, Y. *J. Am. Chem. Soc.* **2003**, *125*, 2408.
(38) Tasi, Y.-C.; Li, S.-C.; Chen, J.-M. *Langmuir* **2005**, *21*, 3653.
(39) Masarwa, M.; Cohen, H.; Meyerstein, D.; Hickman, D. L.; Bakac, A.; Espenson, J. H. *J. Am. Chem. Soc.* **1988**, *110*, 4293.
(40) Belle, C.; Rammal, W.; Pierre, J.-L. *J. Inorg. Biochem.* **2005**, *99*, 1929.

NL0630539